MATERIALS SCIENCE

Atomically engineered cobaltite layers for robust ferromagnetism

Shengru Chen[1,2]†, Qinghua Zhang[1]†, Xujing Li[2,3,4]†, Jiali Zhao[1], Shan Lin[1,2], Qiao Jin[1,2], Haitao Hong[1,2], Amanda Huon[5,6]‡, Timothy Charlton[5], Qian Li[7], Wensheng Yan[7], Jiaou Wang[3], Chen Ge[1], Can Wang[1,2,8], Baotian Wang[3,4], Michael R. Fitzsimmons[5,9], Haizhong Guo[10], Lin Gu[1,2,8]§, Wen Yin[3,4]*, Kui-juan Jin[1,2,8]*, Er Jia Guo[1,2,8]*

Emergent phenomena at heterointerfaces are directly associated with the bonding geometry of adjacent layers. Effective control of accessible parameters, such as the bond length and bonding angles, offers an elegant method to tailor competing energies of the electronic and magnetic ground states. In this study, we construct unit-thick syntactic layers of cobaltites within a strongly tilted octahedral matrix via atomically precise synthesis. The octahedral tilt patterns of adjacent layers propagate into cobaltites, leading to a continuation of octahedral tilting while maintaining substantial misfit tensile strain. These effects induce severe rumpling within an atomic plane of neighboring layers, further triggering the electronic reconstruction between the splitting orbitals. First-principles calculations reveal that the cobalt ions transit to a higher spin state level upon octahedral tilting, resulting in robust ferromagnetism in ultrathin cobaltites. This work demonstrates a design methodology for fine-tuning the lattice and spin degrees of freedom in correlated quantum heterostructures by exploiting epitaxial geometric engineering.

INTRODUCTION

Heterointerfaces are connected by chemical bonds between dissimilar classes of materials (1). Corner-shared octahedral, along with metal-oxygen bonds, constitute the framework of oxide heterostructures (2–4). Conventionally, the most effective means to tune the lattice degree of freedom in a correlated material is to change the misfit strain or shear strain induced by substrates, buffer layers, capping layers, or crystal symmetry (5–10). Advances in the thin-film deposition method have enabled the atomically assembling of heterointerfaces by selectively fabricating oxide layers with different octahedral rotation patterns (11, 12). This phenomenon provides the octahedral rotation, which directly affects the bonding angle (β_{B-O-B}) and bond length (r_{B-O}), as an independent geometric constraint to tune the lattice structure. Interfacial control of the oxygen coordination environment allows an octahedra to rotate, thereby retaining the octahedra of neighboring layers across interfaces and enabling functional properties. This methodology has been effectively applied

to modify the magnetic anisotropy of $SrRuO_3$ (13–16), $La_{2/3}Sr_{1/3}MnO_3$ (17, 18), and La(Nd, Sm)NiO_3 (19–21) thin layers. Similarly, the electronic states of transition metal ions also vary with structural modifications induced by octahedral rotations. The balance between crystal field energy ($\Delta_{CF} \propto r_{B-O}^{-5}$), intra-atomic exchange interaction energy (Δ_{ex}), and bandwidth ($W \propto r_{B-O}^{-3.5} \cos(\pi - \beta_{B-O-B})$) not only substantially alters band structures but also affects the ground state of spin and orbital orders (22, 23). Thus, the octahedral rotation in oxide heterostructures offers a promising strategy to nanoengineer physical properties that are not observed in the bulk constituents or thick layers.

Rare earth scandates typically have heavily distorted orthorhombic perovskite structures. The single crystals of scandates are commonly used as substrates for epitaxial ferroelectric and ferromagnetic (FM) thin-film growth (24–28). The lattice of scandates is derived from the ideal cubic structure by tilting of ScO_6 octahedra along the $[110]_{pc}$ and $[001]_{pc}$ directions of pseudo-cubic unit cells (u.c.) (29, 30). For instance, the crystal structure of $DyScO_3$ (DSO) is shown in Fig. 1A. Dysprosium (Dy) atoms are surrounded by eight scandium-oxygen (ScO_6) octahedra. The octahedra are heavily tilted in response to the occupancy of A-site by a Dy cation, which is smaller than that required to form the ideal structure. The octahedral tilting reduces the crystalline symmetry to a *Pbnm* space group (31, 32). Theoretically, the tilting angle of ScO_6 octahedra in DSO, determined by crystal electrical field calculations, is up to ~25° (33), which is one of the largest octahedral tilting angles in perovskite oxides in the literature. In this work, we use this heavily tilted octahedral matrix in DSO to modify the octahedral tilt in the neighboring $LaCoO_3$ (LCO) layers, exhibiting an active spin-state transition upon structural distortions. We demonstrate that tensile strain induced by substrates and interlayer-mediated octahedral tilt is simultaneously present in synthetic atomic-thin cobaltites. This approach successfully modifies electronic states by changing the bonding geometry. Robust large ferromagnetism is achieved in the single unit-cell LCO, which is nonmagnetic in its original state. The propagation of

[1]Beijing National Laboratory for Condensed Matter Physics and Institute of Physics, Chinese Academy of Sciences, Beijing 100190, China. [2]University of Chinese Academy of Sciences, Beijing 100049, China. [3]Institute of High Energy Physics, Chinese Academy of Sciences, Beijing 100049, China. [4]Spallation Neutron Source Science Center, Dongguan 523803, China. [5]Neutron Scattering Division, Oak Ridge National Laboratory, Oak Ridge, TN 37831, USA. [6]Department of Mathematics, Physics, and Statistics, University of the Sciences, Philadelphia, PA 19104, USA. [7]National Synchrotron Radiation Laboratory, University of Science and Technology of China, Hefei 230029, China. [8]Songshan Lake Materials Laboratory, Dongguan, Guangdong 523808, China. [9]Department of Physics and Astronomy, University of Tennessee, Knoxville, TN 37996, USA. [10]Key Laboratory of Material Physics, Ministry of Education, School of Physics and Microelectronics, Zhengzhou University, Zhengzhou 450001, China.
*Corresponding author. Email: yinwen@ihep.ac.cn (W.Y.); kjjin@iphy.ac.cn (K.-j.J.); ejguo@iphy.ac.cn (E.J.G.)
†These authors contribute equally to this work.
‡Present address: Department of Physics, Saint Joseph's University, Philadelphia, PA 19131, USA.
§Present address: National Center for Electron Microscopy in Beijing, Tsinghua University, Beijing 100084, China; School of Materials Science and Engineering, Tsinghua University, Beijing, 100084, China.
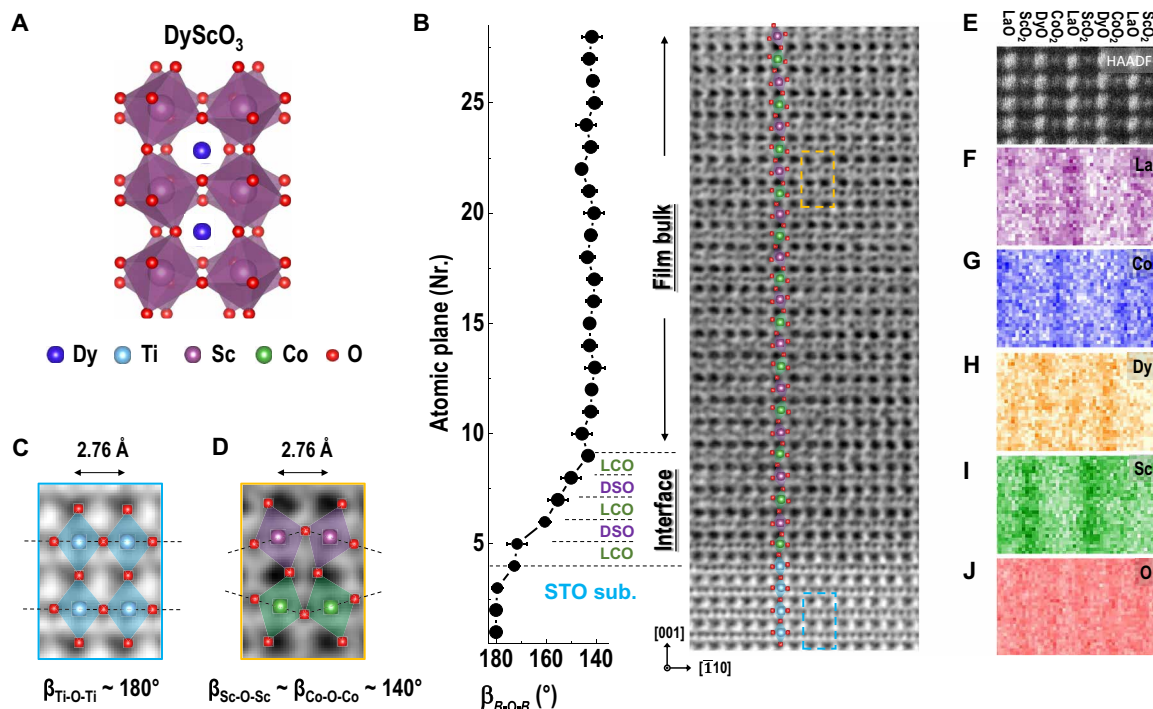
Fig. 1. Structural characterizations of a single unit-cell LCO superlattice. (**A**) Crystallographic structure of bulk $DyScO_3$, illustrating the heavily tilted octahedra within the framework. (**B**) Cross-sectional annular bright-field (ABF) STEM image of a D_1L_1 superlattice (SL). The image was taken along the pseudo-cubic $[110]_{pc}$ zone axis. The layer position–dependent bonding angle ($\beta_{B\text{-}O\text{-}B}$) is shown on the left of the ABF image, where B represents the body-center cations (Co and Sc). $\beta_{B\text{-}O\text{-}B}$ was calculated by averaging bonding angles from atomic planes. Error bars represent 1 SD. (**C** and **D**) Zoomed-in representative oxygen octahedra in STO and LCO (DSO) layers marked in blue and yellow dashed squares in (B), respectively. Schematic illustrations indicate the orientations of octahedral tilts. (**E**) HAADF STEM image of a selected area from D_1L_1 SL. The colored panels show the integrated EELS intensities of (**F**) La M-edge, (**G**) Co L-edge, (**H**) Dy M-edge, (**I**) Sc L-edge, and (**J**) O K-edge from the same region shown in (E).

octahedral tilt in long-range ordering suggests that this methodology can be readily applied to manipulate lattice-orbital interactions in other correlated heterogeneity materials.

RESULTS

DSO_n/LCO_m (D_nL_m) superlattices (SLs) were grown on single crystalline (001)-oriented $SrTiO_3$ (STO) substrates by pulsed laser deposition, where n and m represent the numbers of unit cells. The DSO/LCO bilayers in all SLs were repeated 10 times along the growth direction. X-ray diffraction (XRD) θ-2θ scans demonstrate that all SLs are single phase, and reciprocal space mapping results show that all SLs are epitaxially grown with high crystalline quality and coherently strained to STO substrates (figs. S1 to S3). The DSO (a_o = 5.714 Å, b_o = 5.438 Å, and c_o = 7.897 Å) layers are $[001]_{pc}$-oriented (refers to the $[110]_o$ orientation in orthorhombic indices), where o and pc represent the orthorhombic and pseudo-cubic notation, respectively (*34*). The coherently grown DSO layers underwent a compressive strain of ~1.1% caused by the STO single-crystal substrates, further increasing the octahedral tilt toward the in-plane direction (*35*). The real-space distorted lattice structure is visualized by atomically resolved scanning transmission electron microscopy (STEM). Figure 1B shows a cross-sectional annular bright-field (ABF) STEM image of D_1L_1 SL. The STEM measurements were taken along the $[110]_{pc}$ zone axis, enabling the direct quantification of the BO_6 (B = Sc, Co, and Ti) octahedral tilt. The single unit-cell LCO layers are sandwiched between two DSO layers. The octahedra of

LCO are forced to follow the DSO's octahedral tilt character. The crystalline structure of simplified octahedra in DSO and LCO is schematically shown in Fig. 1B. In-phase versus out-of-phase octahedral tilts occur along the film growth direction. Simultaneously, the atomic plane within DSO or LCO experiences severe rumpling caused by octahedral tilts. The precise atomic column positions were estimated using Gaussian fittings (fig. S4), from which we could obtain the layer position–dependent $\beta_{B\text{-}O\text{-}B}$ across the interfaces, as summarized in Fig. 1B. In the interface regime, the $\beta_{B\text{-}O\text{-}B}$ decreases rapidly from $\beta_{Ti\text{-}O\text{-}Ti}$ ~ 180° in STO substrates. After the first five unit cells in SL, the octahedral tilt reduces to nearly a constant value $\beta_{B\text{-}O\text{-}B}$ ~ 140°. The coherency could be stabilized up to tens of bilayer repeats. Direct comparison of nontilted and tilted octahedra in STO substrates and DSO/LCO SLs is shown in Fig. 1 (C and D). A high-angle annular dark-field (HAADF) STEM image (Fig. 1E), along with electron energy-loss spectroscopy (EELS) maps (Fig. 1, F to J) and energy-dispersive x-ray (EDX) spectroscopy mapping (fig. S5), is recorded from a selected region in D_1L_1 SL. Atomic ordering in different chemical components (La, Co, Dy, Sc, and O) confirms the designed growth sequence. The chemical intermixing across the interfaces is less than two atomic planes. SL exhibits ultrasharp interfaces as evidenced by HAADF STEM images and periodic Bragg peaks in XRD curves. These structural characterizations demonstrate that the non-FM spacing layers act effectively as a template for engineering the octahedral tilting patterns of adjacent layers.

The magnetic properties of DSO/LCO SLs were characterized using a superconducting quantum interference device (SQUID)

magnetometer. Field-cooled magnetization versus temperature (*M-T*) curves of SLs indicate a paramagnetic (PM)–to–FM phase transition at Curie temperature (T_C) ~ 75 K (fig. S6). The line shapes of *M-T* curves for SLs are the same as those of LCO single layers, implying that the FM origin is from LCO ultrathin layers. We note that the T_C of SLs is lower than that of an LCO thick film. This fact has been previously observed in other FM oxide films with reduced dimensionality (*36*). Field-dependent magnetization (*M-H*) curves for SLs are shown in Fig. 2A and fig. S5. In contrast to the pure PM response from a DSO single layer (inset of Fig. 2A) (*37*), the *M-H* curve of D_1L_1 SL exhibits an open hysteresis loop with nonzero remnant magnetization (M_r) of ~25 electromagnetic units (emu)/cm^3 and coercive field (H_C) of ~650 Oe. This indicates that the long-range ferromagnetism persists in atomically thin LCO SLs. For a $D_{10}L_{10}$ SL, both M_r and H_C increase to ~32 emu/cm^3 and ~2 kOe, respectively. The increase in the number of magnetic parameters can be attributed to the thicker LCO layers, which can lead to the long-range spin ordering. Figure 2 (B and C) shows the saturation magnetization (M_S) and H_C as a function of the averaged out-of-plane lattice constant of D_nL_{10} SLs for $1 \leq n \leq 10$. The increase of out-of-plane lattice constants in SLs is caused by the increase of DSO layers' number in SLs. We observe large deviations in both curves of SLs as

the lattice constant increases. The in-plane H_C reaches the maximum value for SL (*m* = 3). The out-of-plane lattice constant of this SL is ~3.81 Å (*38*), which is equal to the pseudo-cubic lattice constant of bulk LCO. The observed anomaly in the magnetic properties indicates a remarkable structural modification effect.

In addition, although macroscopic magnetization measurements provide solid evidence on the ferromagnetism in atomically thin LCO, the pronounced PM signals from DSO at low temperatures prevent us from subtracting the exact M_S of LCO. To separate the PM contribution from DSO, we performed polarized neutron reflectometry (PNR) measurements on a $D_{10}L_{10}$ SL to obtain magnetization across the layers of the sample. We choose the $D_{10}L_{10}$ SL as a test model not only because its total magnetization is similar to that of D_1L_1 SL but also because the first Bragg peak appears within the neutron measurement range (*39–41*). The specular neutron reflectivities from spin-up (R^+) and spin-down (R^-) neutrons were collected as a function of wave vector transfer (*q*), as shown in Fig. 2D. The difference between R^+ and R^- is further demonstrated by calculating the spin asymmetry [SA = $(R^+ - R^-)/(R^+ + R^-)$]. Nonzero SA confirms no evidence of antiferromagnetism within the SLs. PNR data were fitted using a model describing the chemical profile obtained from x-ray reflectivity fitting to the same SL (fig. S7)
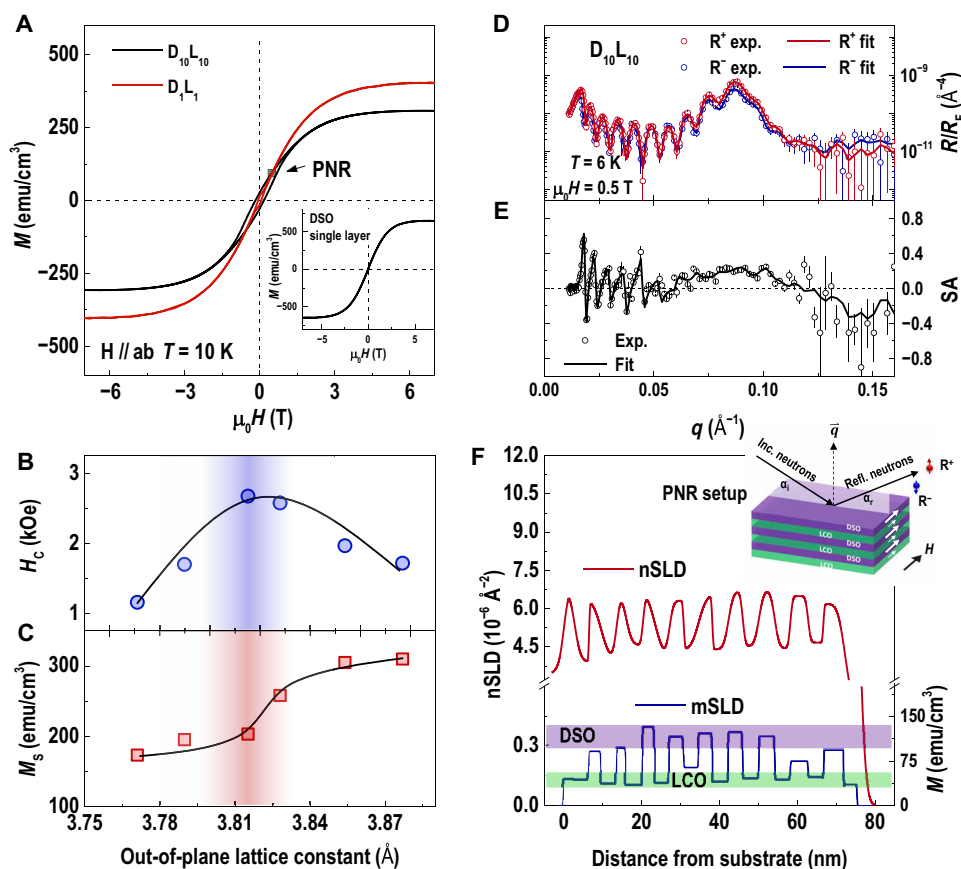

Fig. 2. Magnetic properties of D_nL_m SLs. (**A**) *M-H* loops of D_1L_1 and $D_{10}L_{10}$ SLs. *M-H* loops were recorded at 10 K when a magnetic field was applied along the in-plane direction. Inset shows the *M-H* curve of a DSO single layer. (**B**) Coercive fields (H_C) and (**C**) saturation magnetization (M_S) of D_nL_m SLs are plotted as a function of the out-of-plane lattice constant. M_S was calculated using the total thickness of SLs. (**D**) Normalized neutron reflectivity curves and (**E**) SA curve of a $D_{10}L_{10}$ SL for spin-up (R^+)–polarized and spin-down (R^-)–polarized neutrons are shown as a function of the wave vector transfer *q*. (**F**) Nuclear scattering length density (nSLD) and magnetic scattering length density (mSLD) depth profiles of $D_{10}L_{10}$ SL. Magnetization of individual layers was calculated and compared with magnetometry data in (A). The inset of (F) displays the PNR measurement setup.

(42). Open symbols and solid lines in Fig. 2 (D and E) represent the experimental data and best fits, respectively. PNR fitting yields a reasonably small figure of merit value of ~0.05, indicating that the optimized chemical and magnetic models are applied. Figure 2F shows the depth profiles of nuclear and magnetic scattering length densities of $D_{10}L_{10}$ SL. The best fits show that the spins in LCO align parallel to that in DSO under applied magnetic fields. We calculate the in-plane magnetization of LCO and DSO layers within SLs. The first two bilayers exhibit comparably smaller magnetization than the rest in SLs. These variations are consistent with the observations of different octahedral tilts in the interfacial regime of SLs. From our analysis of the PNR results, we obtain $M_{DSO} = 122 \pm 20$ emu/cm^3 and $M_{LCO} = 43 \pm 12$ emu/cm^3, respectively, under a magnetic field of 0.5 T at 6 K. The obtained M_{LCO} by PNR agrees well with our SQUID results in Fig. 2A.

Next, we analyze the impact of structural distortions on the electronic states by elemental-specific x-ray absorption spectroscopy (XAS). Figure 3A shows XAS at O K- and Co L-edges for D_1L_1 SL. The reference XAS curves from an LCO tensile-strained film (43) and an HSrCoO$_{2.5}$ thin film (44) are present for direct comparison. XAS at Co L-edges consistently shows that the oxidization state of Co ions in SL is +3 with a negligible energy shift, suggesting no external effects, such as charge transfer across the heterointerfaces (45, 46) or any defect formation present in SLs (47). In addition, the features at XAS O K-edges provide indirect but convenient means to reflect the unoccupied orbitals of transition metal ions in SLs. The distinct pre-peaks at ~530 eV correspond to the excitations from the O 1s state to the O 2p-Co 3d hybridized state (48) Thus, the XAS results suggest that the t_{2g} bands in Co 3d orbitals are not fully occupied for D_1L_1 SL. In contrast, the absence of pre-peaks in HSrCoO$_{2.5}$ demonstrates that its t_{2g} bands are completely occupied, similar to bulk LCO (49). Figure 3B shows the schematic of electronic structures and spin states as a response to the change in Δ_{CF} and W, i.e., β_{B-O-B} and r_{B-O}. For the unstrained bulk LCO, degenerate orbitals are expected. Applying epitaxial strain would reduce orbital degeneracy and decrease the overlap between d orbitals and neighboring oxygen orbitals, thereby reducing the energy of these orbitals. For tensile-strained LCO layers in D_1L_1 SL, the energy of $d_{x^2-y^2}$ orbital is lower than that of $d_{3z^2-r^2}$ orbital (Fig. 3C). Electrons excited from t_{2g} bands preferentially occupy the $d_{x^2-y^2}$ orbital rather than the $d_{3z^2-r^2}$ orbital. The number of unoccupied states in the $d_{3z^2-r^2}$ orbital is larger than that in the $d_{x^2-y^2}$ orbital. The calculated x-ray linear dichroism (XLD) at Co L-edges confirms the expected anisotropic orbital occupancy in e_g orbitals (Fig. 3D) (50–52) In D_1L_1 SL, $\beta_{Co-O-Co}$ decreases from a flattened bond, further reducing the e_g bandwidth, which increases the number of occupied orbital states. The spin state of Co ions in D_1L_1 SL is presumably higher than that of thick LCO tensile-strained films with the flattened $\beta_{Co-O-Co}$. The evolution of orbital occupation states with octahedral tilt provides a reasonable explanation for the observed ferromagnetism in ultrathin LCO layers.

To validate our atomic engineering strategy on octahedral parameters, we grew another two sets of atomic-thin LCO SLs using LaFeO$_3$ (LFO) and STO to replace DSO. Because our SLs have nearly identical small film thicknesses, all layers are coherently grown on the STO substrates. The LCO layers suffer the identical tensile strain from the substrates. Applying other materials having different octahedral tilt patterns inevitably adds another degree of freedom to further tune the β_{B-O-B}, i.e., the spin states of Co ions. To this end, the LFO single crystals have an orthorhombic structure with an identical $a^-a^-c^+$ tilt pattern in Glazer notation, as DSO (53). The lattice constant difference between DSO and LFO is only ~0.5%. Therefore, we expect a similar octahedral tilt in LFO from a high-symmetry cubic parent structure, accommodated by combined in-phase octahedral
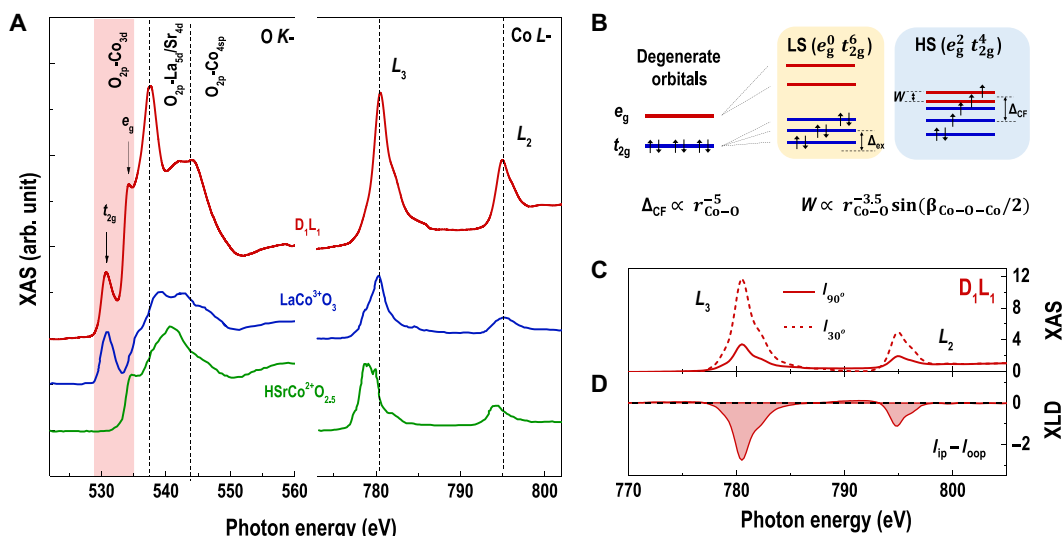
Fig. 3. Increased e_g orbital occupancy in single unit-cell LCO SL. (A) Elemental-specific XAS at O K- and Co L-edges for D_1L_1 SL. The shadow area in XAS O K-edges represents the electronic hybridization between O 2p and Co 3d orbitals. Reference data from an FM LaCo^{3+}O$_3$ tensile-strained thin film and an FM thin HSrCo^{2+}O$_{2.5}$ film are shown for direct comparison (43, 44). (B) Electronic structure of Co 3d orbital state. Degenerate e_g and t_{2g} orbitals split into two and three levels, respectively. Low-spin (LS) and high-spin (HS) states are effectively controlled by the interplay between Δ_{CF} and W. (C) Polarization-dependent XAS at Co L-edges for D_1L_1 SL. The sample's scattering plane was rotated at angles of 90° and 30° with respect to the incident direction of an x-ray beam. Unoccupied in-plane orbital states are proportional to $I_{ip} = I_{90°}$, whereas unoccupied out-of-plane orbital states can be calculated by $I_{oop} = (I_{90°} - I_{30°} \cdot \sin^2 30°)/\cos^2 30°$. (D) XLD, calculated from ($I_{ip} - I_{oop}$), of D_1L_1 SL. The clear XLD signal demonstrates an asymmetric electronic occupancy in Co 3d e_g orbitals.

tilting about the orthorhombic *a* axis and out-of-phase tilt about the orthorhombic *b* and *c* axes (figs. S8 and S9). The octahedral tilting effectively and structurally modifies LCO layers. Figure 4A shows the *M-H* hysteresis loop for an LFO$_1$/LCO$_1$ (F$_1$L$_1$) SL. Compared to the *M-H* loop for D$_1$L$_1$ SL, both SLs exhibit nearly identical H_C under the same measuring conditions. This is a strong indication that the enhanced magnetic properties in both SLs are associated with octahedral tilt induced by adjacent layers. We determined that both valence states of Fe and Co ions have +3, inhibiting interfacial charge transfer (fig. S10). Presumably, the LFO layers maintain their anti-FM ordering of the bulk, where five 3*d* electrons are arranged in a high-spin (HS) state $t_{2g}^3 e_g^2$ and are coupled across the structures through superexchange interactions (*54*). The FM character of LCO was reinforced by measuring elemental-specific XAS and x-ray magnetic circular dichroism (XMCD) spectra for Co *L*-edges (Fig. 4, B and C). Therefore, the magnetization of F$_1$L$_1$ SL is normalized to the total thickness of LCO layers. The M_S of F$_1$L$_1$ SL reaches ~110 emu/cm^3 (~0.7 μ_B/Co). This is the highest value of the net magnetic moment in atomic-thin LCO layers reported to date. Another control experiment was conducted with a STO$_1$/LCO$_1$ (S$_1$L$_1$) SL, where STO has an $a^0a^0a^0$ nontilted pattern (*17*). The octahedral tilt in LCO layers is strongly suppressed, as shown in the inset of Fig. 4A. The crystalline symmetry of LCO in S$_1$L$_1$ SL transits into a tetragonal-like structure. The spin state of Co^{3+} ions would be lower than that in heavily tilted octahedra. Thus, the magnetization of S$_1$L$_1$ SL is negligible. The obvious discrepancy between the two cases (LCO/LFO versus LCO/STO) provides strong evidence for octahedral distortion-mediated electronic states. Apparently, the intrinsic structural modification using the spacing layer is a different but effective means to influence the orbital occupancies. The consistent results of changing the active spin states of cobalt ions were reported to use the intrinsic crystal symmetry or the extrinsic hydrostatic pressure (*15*, *55–57*).

To further clarify the effects of octahedral titling and lattice distortion on the spin state of LCO, we performed first-principles calculations within the framework of density functional theory (*58*, *59*). Critical parameters, e.g., the on-site Coulomb interaction

(*U*) and exchange interaction (*J*), were chosen on the basis of the ground states of material systems (*60*, *61*). The calculation details and selected critical parameters are summarized in fig. S11. Both 2 × 2 × 2 and 3 × 3 × 3 supercells are constructed to simulate the structure of our SLs (fig. S12). The structures were optimized with in-plane (biaxially tensile) lattice parameters of LCO fixed to that of STO substrates. The out-of-plane lattice constants of LCO were optimized by reducing the free energy of the geometric structure (table S1). The initial lattice structure of LCO is nearly identical for both spin states (*62*, *63*). The octahedral tilt increases when LCO is proximate to DSO or LFO, whereas the octahedral tilt in LCO is strongly suppressed when it is sandwiched between two STO layers. We calculated the potential energies of the low-spin (LS) configuration (E_{LS}) and intermediate-spin configuration (E_{IS}) (fig. S13). Figure 5A depicts the energy difference ($\Delta E = E_{IS} - E_{LS}$) between the two spin configurations as a function of octahedral rotation amplitude. ΔE is close to zero when the octahedral rotation amplitude is less than 2%. An increase in the rotation amplitude negates ΔE, suggesting that electrons prefer to occupy HS states rather than LS states. The critical rotation amplitude for the spin-state transition reduces gradually when the LCO unit cell elongates along the growth direction. These results are consistent with our experimental findings that octahedral rotation enhances the macroscopic magnetization of atomic-thin LCO layers. Furthermore, we calculated the average moment of DSO/LCO stacks as a function of the out-of-plane lattice constant, as shown in Fig. 5B. The magnetic moment of these stackings changes nonlinearly with structural elongation (increase of octahedral tilting angle), which agrees well with our experimental observations (Fig. 2C). The theoretical calculations reveal a strong correlation between octahedral rotation and electronic spin states in LCO, explaining the origin of macroscopic magnetization in atomic-thin LCO layers.

DISCUSSION
In summary, we demonstrate the tuning of electronic states in atomic-thin LCO by octahedral engineering. The octahedral tilt in
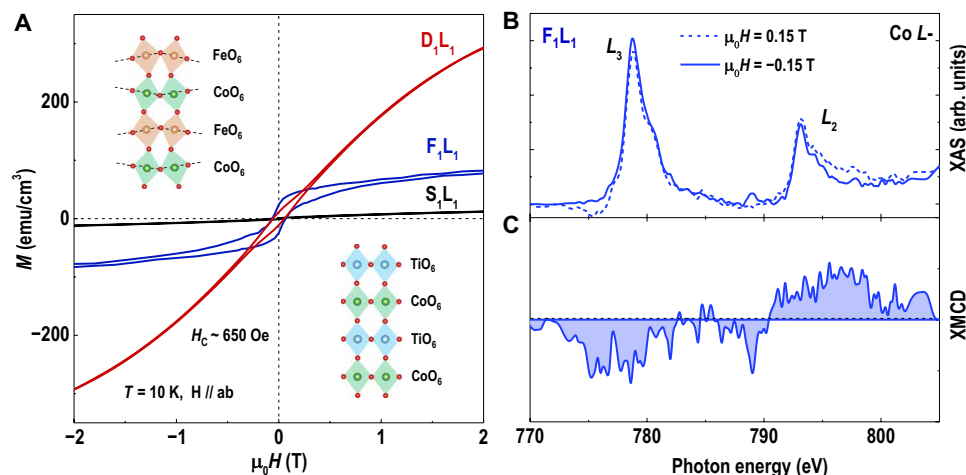
Fig. 4. Manipulation of magnetic states in single unit-cell SLs via octahedral rotation. (**A**) *M-H* loops of D$_1$L$_1$, F$_1$L$_1$, and S$_1$L$_1$ SLs. Magnetization measurements were performed at 10 K and in an in-plane magnetic field. Both D$_1$L$_1$ and F$_1$L$_1$ SLs exhibit identical H_C ~ 650 Oe. Insets show octahedral rotation patterns in D$_1$L$_1$ and F$_1$L$_1$ SLs. (**B**) XAS and (**C**) XMCD at Co *L*-edges for a F$_1$L$_1$ SL. XAS spectra were collected by applying a circularly polarized x-ray beam at 77 K under magnetic fields of +0.15 T (dashed line) and −0.15 T (solid line). XMCD spectra were calculated from the difference between two XAS spectra, demonstrating a clear magnetic signal from Co ions.
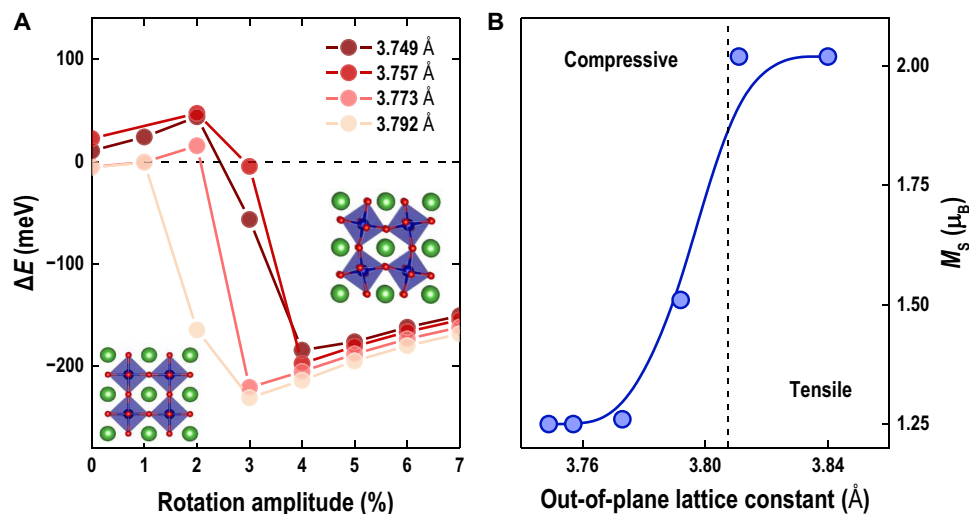
Fig. 5. First-principles calculations on the electronic states of SLs at different rotation angles and under different lattice distortions. (**A**) The energy difference ($\Delta E = E_{IS} - E_{LS}$) between intermediate-spin (IS) and LS states as a function of the octahedral rotation amplitude. The rotation amplitude varying from 0 to 7% represents $\beta_{Co-O-Co}$ changing from 180° to 153°, respectively. Insets show the schematic crystal structures of 2×2 LCO atomic layers with and without octahedral tilt. (**B**) Nonlinear change of magnetic moments in LCO with out-of-plane lattice constants. Lattice deformation is constrained by ISODISTORT.

LCO can be modified by neighboring layers and reaches a small Co—O—Co bonding angle of ~140°, which has not been reported previously. The heavily distorted octahedra trigger the active spin-state transition, resulting in a record-high magnetic moment in single unit-cell thick LCO layers. Effective manipulation of octahedral parameters in functional oxides enables the study of the impact of spin-orbital correlations in terms of magnetoelectric properties, paving a previously unidentified way for controlling the magnetic functionalities that are not present in their bulk forms.

MATERIALS AND METHODS
Synthesis of SLs
The LCO-based SLs were grown on (001)-oriented STO substrates (Hefei Kejing Materials Technology Co. Ltd) using pulsed laser deposition. The STO substrates were pretreated by HF acid and annealed at 1080°C for 90 min to obtain atomically flat TiO$_2$ termination. The sintered LCO and LFO ceramics and the STO and DSO single crystals were used as the ablation targets to maintain the highest stoichiometry. All targets have a diameter of 25.4 mm and a thickness of 3 to 5 mm. The SLs were fabricated by alternating two targets for thin-film growth. For all layers, we optimized their growth conditions to be the same and avoided to vary the conditions repeatedly. The substrate's temperature was kept at 750°C, and oxygen partial pressure was maintained at 100 mtorr. The laser furnace was kept ~1 to 1.1 J/cm^2, and the laser repetition was 3 Hz. After the thin-film deposition, the samples were cooled down under the oxygen pressure of 100 torr. The growth rates for each layer were precalibrated by growing individual films with three different thicknesses. The average growth rates were used for the thin-film deposition (40 pulses/u.c. for LCO, 56 pulses/u.c. for LFO, 100 pulses/u.c. for DSO, and 95 pulses/u.c. for STO). The thicknesses of individual layers are controlled precisely by controlling the numbers of laser pulse. With this method, oxide SLs can be fabricated with atomic precision, as demonstrated in previous works (*12, 14, 15, 19, 40, 46, 64*).

Structural and basic physical property characterizations
XRD and reciprocal space mapping (RSM) measurements were carried out using a PANalytical X'Pert3 MRD diffractometer. The macroscopic magnetizations of all SLs were measured using a SQUID magnetometer. All measurements were performed by applying in-plane magnetic fields. The *M-T* curves were recorded during the sample warm-up process after field-cooled at 1 kOe. The *M-H* hysteresis loops were recorded at 10 K. The *M-H* loops were obtained by subtracting the diamagnetic signals from STO layers and substrates. Unfortunately, the PM signals from DSO ultrathin layers cannot be subtracted because the PM contributions from DSO vary with layer thickness. Therefore, the magnetizations of DSO/LCO SLs were normalized to the total thickness of SLs. The LFO is an antiferromagnet and does not contribute to the measured magnetization, thus the magnetizations of LFO/LCO SLs were normalized to the total thickness of LCO layers.

STEM measurements and analysis
Cross-sectional TEM specimens of DSO/LCO and LFO/LCO SLs were prepared using Ga$^+$ ion milling after the mechanical thinning. HAADF and ABF imaging were carried out in scanning mode. The measurements were taken using a JEM ARM 200CF microscope at the Institute of Physics, Chinese Academy of Sciences. The ABF images were taken along the pseudo-cubic [110]$_{pc}$ zone axis to directly visualize the oxygen atoms. The results help us to analyze the octahedral tilt in the lattices. The atomic positions of Co and O ions were determined by fitting the intensity peaks with Gaussian function. The parameters of this model, including the atomic column position, the height, and the width of the Gaussian peak, have been calculated using the least squares estimator (for details, see fig. S4). Therefore, the bond length and bonding angles of Co—O—Co (Sc—O—Sc) bonds can be obtained precisely. The obtained values were averaged over the single atomic plane within the ABF image. Error bars were extracted by calculating the SD value. The elemental-specific EELS mappings and dual-type EDX spectroscopy mappings were performed by integrating the signals from a selected region

after subtracting the exponent background using power law. All data were analyzed using Gatan Micrograph software.

PNR measurements

The PNR experiment on $D_{10}L_{10}$ SL was performed using the magnetism reflectometer (MR, BL-4A) of Spallation Neutron Source, Oak Ridge National Laboratory (ORNL). The sample was cooled down and measured at 6 K under an in-plane magnetic field of 0.5 T. PNR measurements were conducted in the specular reflection geometry with wave vector transfer (q) perpendicular to the surface plane. q is calculated by $4\pi \sin(\alpha_i)/\lambda$, where α_i is the neutron incident angle and λ is the wavelength of neutron beam. Neutron reflectivities from spin-up (R^+) and spin-down (R^-) neutrons were recorded separately. To better illustrate their differences, the neutron reflectivities were normalized to the asymptotic value of the Fresnel reflectivity ($R_F = 16\pi^2/q^4$). Simultaneously, we calculate the SA using $(R^+ - R^-)/(R^+ + R^-)$. By fitting the PNR data, we obtain the magnetizations of the DSO and LCO layers separately. Please note that we allow the magnetization of DSO layers to vary for each layer during PNR fitting. The SDs of the magnetization values of the layers form the uncertainties of the Ms.

XAS and XMCD measurements

Elemental-specific XAS measurements were performed on SLs at the beamline 4B9B of the Beijing Synchrotron Radiation Facility (BSRF). All spectra were collected at room temperature in total electron yield (TEY) mode. The measurements were performed by changing the incident angle of linearly polarized x-ray beam. The sample's scattering plane was rotated by 30° and 90° with respect to the incoming photons. When the x-ray beam is perpendicular to the surface plane, the XAS signal directly reflects the $d_{x^2-y^2}$ orbital occupancy. While the angle between the x-ray beam and surface plane is 30°, the XAS signal contains orbital information from both $d_{x^2-y^2}$ and $d_{3z^2-r^2}$ orbitals. Therefore, for simplifying the results, the unoccupied in-plane orbital states are proportional to $I_{ip} = I_{90°}$, while the unoccupied out-of-plane orbital states can be calculated by $I_{oop} = (I_{90°} - I_{30°} \cdot \sin^2 30°)/\cos^2 30°$. XLD is calculated by $I_{ip} - I_{oop}$. The XMCD measurements were performed on F_1L_1 SL using circularly polarized x-rays at 77 K in TEY mode. Instead of switching the polarity of x-ray beams, we collected the XAS under the opposite magnetic fields of ±0.15 T. The XMCD signals were obtained by calculating the difference between XAS (+0.15 T) and XAS (−0.15 T).

First-principles calculations

The first-principles calculations were performed within the framework of density functional theory with Perdew-Burke-Ernzerhof exchange-correlation pseudo-potential as implemented in the Vienna Ab Initio Simulation Package. A plane wave representation for the wave function with a cutoff energy of 550 eV was applied. Geometry optimizations were performed using a conjugate gradient minimization until all the forces acting on the ions were less than 0.01 eV/Å per atom. A dense $14 \times 14 \times 14$ Monkhorst-Pack K-point grid was used for calculations. The crystal structures are built using VESTA software. The in-plane lattice parameters of SLs, constrained by our XRD measurements, were fixed to the STO substrate ($a = 3.905$ Å). We use ISODISTORT to analyze the distorted modes and strain states of both experimental and optimized lattice structures. In all cases, we use the highly symmetrical Pm-$3m$ structure to describe the crystal structure of LCO. The pseudo-cubic lattice constant of bulk LCO adapts $a_{pc} = 3.83$ Å, which was obtained from earlier neutron diffraction data. For any applied lattice distortions, each formula unit maintains the same lattice volume same as the experiments. The rotation mode structure with a $2 \times 2 \times 2$ supercell was adopted for the structural simulation. We normalized the rotation amplitude of 7% equals to the octahedral rotation angles $\beta_{Co-O-Co}$ of 154.33° with respect to its cubic structure (the ground states of lattice volume).

SUPPLEMENTARY MATERIALS

Supplementary material for this article is available at https://science.org/doi/10.1126/sciadv.abq3981

REFERENCES AND NOTES

1. J. Mannhart, D. G. Schlom, Oxide interfaces—An opportunity for electronics. *Science* **327**, 1607–1611 (2010).
2. H. Y. Hwang, Y. Iwasa, M. Kawasaki, B. Keimer, N. Nagaosa, Y. Tokura, Emergent phenomena at oxide interfaces. *Nat. Mater.* **11**, 103–113 (2012).
3. S. Das, Y. L. Tang, Z. Hong, M. A. P. Gonçalves, M. R. McCarter, C. Klewe, K. X. Nguyen, F. Gómez-Ortiz, P. Shafer, E. Arenholz, V. A. Stoica, S. L. Hsu, B. Wang, C. Ophus, J. F. Liu, C. T. Nelson, S. Saremi, B. Prasad, A. B. Mei, D. G. Schlom, J. Íñiguez, P. García-Fernández, D. A. Muller, L. Q. Chen, J. Junquera, L. W. Martin, R. Ramesh, Observation of room-temperature polar skyrmions. *Nature* **568**, 368–372 (2019).
4. J. A. Mundy, C. M. Brooks, M. E. Holtz, J. A. Moyer, H. Das, A. F. Rébola, J. T. Heron, J. D. Clarkson, S. M. Disseler, Z. Q. Liu, A. Farhan, R. Held, R. Hovden, E. Padgett, Q. Y. Mao, H. Paik, R. Misra, L. F. Kourkoutis, E. Arenholz, A. Scholl, J. A. Borchers, W. D. Ratcliff, R. Ramesh, C. J. Fennie, P. Schiffer, D. A. Muller, D. G. Schlom, Atomically engineered ferroic layers yield a room-temperature magnetoelectric multiferroic. *Nature* **537**, 523–527 (2016).
5. K. J. Choi, M. Biegalski, Y. L. Li, A. Sharan, J. Schubert, R. Uecker, P. Reiche, Y. B. Chen, X. Q. Pan, V. Gopalan, L. Q. Chen, D. G. Schlom, C. B. Eom, Enhancement of ferroelectricity in strained BaTiO$_3$ thin films. *Science* **306**, 1005–1009 (2004).
6. D. G. Schlom, L. Q. Chen, C. B. Eom, K. M. Rabe, S. K. Streiffer, J. M. Triscone, Strain tuning of ferroelectric thin films. *Annu. Rev. Mat. Res.* **37**, 589–626 (2007).
7. G. Koster, M. Huijben, G. Rijnders, *Epitaxial Growth of Complex Metal Oxides* (Woodhead Publishing Series in Electronic and Optical Materials, Elsevier, 2015).
8. S. Thomas, B. Kuiper, J. Hu, J. Smit, Z. Liao, Z. Zhong, G. Rijnders, A. Vailionis, R. Wu, G. Koster, J. Xia, Localized control of Curie temperature in perovskite oxide film by capping-layer-induced octahedral distortion. *Phys. Rev. Lett.* **119**, 177203 (2017).
9. S. G. Jeong, T. Min, S. Woo, J. Kim, Y. Q. Zhang, S. W. Cho, J. Son, Y. M. Kim, J. H. Han, S. Park, H. Y. Jeong, H. Ohta, S. Lee, T. W. Noh, J. Lee, W. S. Choi, Phase instability amid dimensional crossover in artificial oxide crystal. *Phys. Rev. Lett.* **124**, 026401 (2020).
10. J. M. Ok, N. Mohanta, J. Zhang, S. Yoon, S. Okamoto, E. S. Choi, H. Zhou, M. Briggeman, P. Irvin, A. R. Lupini, Y.-Y. Pai, E. Skoropata, C. Sohn, H. Li, H. Miao, B. Lawrie, W. S. Choi, G. Eres, J. Levy, H. N. Lee, Correlated oxide Dirac semimetal in the extreme quantum limit. *Sci. Adv.* **7**, eabf9631 (2021).
11. H. Boschker, T. Harada, T. Asaba, R. Ashoori, A. V. Boris, H. Hilgenkamp, C. R. Hughes, M. E. Holtz, L. Li, D. A. Muller, H. Nair, P. Reith, X. Renshaw Wang, D. G. Schlom, A. Soukiassian, J. Mannhart, Ferromagnetism and conductivity in atomically thin SrRuO$_3$. *Phys. Rev. X* **9**, 011027 (2019).
12. S. Li, Q. H. Zhang, S. Lin, X. H. Sang, R. F. Need, M. A. Roldan, W. J. Cui, Z. Y. Hu, Q. Jin, S. Chen, J. L. Zhao, J. O. Wang, J. S. Wang, M. He, C. Ge, C. Wang, H. B. Lu, Z. P. Wu, H. Z. Guo, X. Tong, T. Zhu, B. Kirby, L. Gu, K. J. Jin, E. J. Guo, Strong ferromagnetism achieved via breathing lattices in atomically thin cobaltites. *Adv. Mater.* **33**, 2001324 (2021).
13. D. Kan, R. Aso, R. Sato, M. Haruta, H. Kurata, Y. Shimakawa, Tuning magnetic anisotropy by interfacial engineering the oxygen coordination environment in a transition metal oxide. *Nat. Mater.* **15**, 432–437 (2016).
14. Z. Cui, A. J. Grutter, H. Zhou, H. Cao, Y. Q. Dong, D. A. Gilbert, J. Y. Wang, Y. S. Liu, J. J. Ma, Z. P. Hu, J. H. Guo, J. Xia, B. J. Kirby, P. Shafer, E. Arenholz, H. H. Chen, X. F. Zhai, Y. L. Lu, Correlation-driven eightfold magnetic anisotropy in a two-dimensional oxide monolayer. *Sci. Adv.* **6**, eaay0114 (2020).
15. S. G. Jeong, G. Han, S. Song, T. Min, A. Y. Mohamed, S. Park, J. Lee, H. Y. Jeong, Y. M. Kim, D. Y. Cho, W. S. Choi, Propagation control of octahedral tilt in SrRuO$_3$ via artificial heterostructuring. *Adv. Sci.* **7**, 2001643 (2020).
16. S. Lin, Q. Zhang, X. H. Sang, J. L. Zhao, S. Cheng, A. Huon, Q. Jin, S. Chen, S. R. Chen, W. J. Cui, H. Z. Guo, M. He, C. Ge, C. Wang, J. Wang, M. R. Fitzsimmons, L. Gu, T. Zhu, K. J. Jin, E. J. Guo, Dimensional control of octahedral tilt in SrRuO$_3$ via infinite-layered oxides. *Nano Lett.* **21**, 3146–3154 (2021).

17. Z. Liao, M. Huijben, Z. Zhong, N. Gauquelin, S. Macke, R. J. Green, S. Van Aert, J. Verbeeck, G. Van Tendeloo, K. Held, G. A. Sawatzky, G. Koster, G. Rijnders, Controlled lateral anisotropy in correlated manganite heterostructures by interface-engineered oxygen octahedral coupling. *Nat. Mater.* **15**, 425–431 (2016).

18. M. Huijben, G. Koster, Z. L. Liao, G. Rijnders, Interface-engineered oxygen octahedral coupling in manganite heterostructures. *Appl. Phys. Rev.* **4**, 041103 (2017).

19. A. V. Boris, Y. MAtiks, E. Benckiser, A. Frano, P. Popovich, V. Hinkov, P. Wochner, M. Castro-colin, E. Detemple, V. K. Malik, C. Bernhard, T. Prokscha, A. Suter, Z. Salman, E. Morenzoni, G. Cristiani, H.-U. Habermeier, B. Keimer, Dimensionality control of electronic phase transitions in nickel-oxide superlattices. *Science* **332**, 937–940 (2011).

20. Z. Liao, N. Gauquelin, R. J. Green, K. Müller-Caspary, I. Lobato, L. Li, S. Van Aert, J. Verbeeck, M. Huijben, M. N. Grisolia, V. Rouco, R. El Hage, J. E. Villegas, A. Mercy, M. Bibes, P. Ghosez, G. A. Sawatzky, G. Rijnders, G. Koster, Metal–insulator-transition engineering by modulation tilt-control in perovskite nickelates for room temperature optical switching. *Proc. Natl. Acad. Sci. U.S.A.* **115**, 9515–9520 (2018).

21. C. Domínguez, A. B. Georgescu, B. Mundet, Y. Zhang, J. Fowlie, A. Mercy, A. Waelchli, S. Catalano, D. T. L. Alexander, P. Ghosez, A. Georges, A. J. Millis, M. Gibert, J.-M. Triscone, Length scales of interfacial coupling between metal and insulator phases in oxides. *Nat. Mater.* **19**, 1182–1187 (2020).

22. D. Meng, H. Guo, Z. Cui, C. Ma, J. Zhao, J. Lu, H. Xu, Z. Wang, X. Hu, Z. Fu, R. Peng, J. Guo, X. Zhai, G. J. Brown, R. Knize, Y. Lu, Strain-induced high-temperature perovskite ferromagnetic insulator. *Proc. Natl. Acad. Sci. U.S.A.* **115**, 2873–2877 (2018).

23. V. V. Mehta, N. Biskup, C. Jenkins, E. Arenholz, M. Varela, Y. Suzuki, Long-range ferromagnetic order in LaCoO$_{3-\delta}$ epitaxial films due to the interplay of epitaxial strain and oxygen vacancy ordering. *Phys. Rev. B* **91**, 144418 (2015).

24. Y. H. Chu, Q. He, C. H. Yang, P. Yu, L. W. Martin, P. Shafer, R. Ramesh, Nanoscale control of domain architectures in BiFeO$_3$ thin films. *Nano Lett.* **9**, 1726–1730 (2009).

25. F. Johann, A. Morelli, D. Biggemann, M. Arredondo, I. Vrejoiu, Epitaxial strain and electric boundary condition effects on the structural and ferroelectric properties of BiFeO$_3$ films. *Phys. Rev. B* **84**, 094105 (2011).

26. J. Bertinshaw, R. Maran, S. J. Callori, V. Ramesh, J. Cheung, S. A. Danilkin, W. T. Lee, S. Hu, J. Seidel, N. Valanoor, C. Ulrich, Direct evidence for the spin cycloid in strained nanoscale bismuth ferrite thin films. *Nat. Commun.* **7**, 12664 (2016).

27. S.-Q. Xu, Y. Zhang, H.-Z. Guo, W.-P. Geng, Z.-L. Bai, A.-Q. Jiang, Improved polarization retention of BiFeO$_3$ thin films using GdScO$_3$ (110) substrates. *Chinese Phys. Lett.* **34**, 027014 (2017).

28. I. Gross, W. Akhtar, V. Garcia, L. J. Martínez, S. Chouaieb, K. Garcia, C. Carrétéro, A. Barthélémy, P. Appel, P. Maletinsky, J.-V. Kim, J. Y. Chauleau, N. Jaouen, M. Viret, M. Bibes, S. Fusil, V. Jacques, Real-space imaging of non-collinear antiferromagnetic order with a single-spin magnetometer. *Nature* **549**, 252–256 (2017).

29. O. Chaix-Pluchery, D. Sauer, J. Kreisel, Temperature-dependent Raman scattering of DyScO$_3$ and GdScO$_3$ single crystals. *J. Phys. Conden. Matter.* **22**, 165901 (2010).

30. X. Ke, C. Adamo, D. G. Schlom, M. Bernhagen, R. Uecker, P. Schiffer, Low temperature magnetism in the perovskite substrate DyScO$_3$. *Appl. Phys. Lett.* **94**, 152503 (2009).

31. R. P. Liferovich, R. H. Mitchell, A structural study of ternary lanthanide orthoscandate perovskites. *J. Solid State Chem.* **177**, 2188–2197 (2004).

32. R. Uecker, B. Velickov, D. Klimm, R. Bertram, M. Bernhagen, M. Rabe, M. Albrecht, R. Fornari, D. G. Schlom, Properties of rare-earth scandate single crystals (Re=Nd-Dy). *J. Cryst. Growth* **310**, 2649–2658 (2008).

33. L. S. Wu, S. E. Nikitin, M. Frontzek, A. I. Kolesnikov, G. Ehlers, M. D. Lumsden, K. A. Shaykhutdinov, E.-J. Guo, A. T. Savici, Z. Gai, A. S. Sefat, A. Podlesnyak, Magnetic ground state of the Ising-like antiferromagnet DyScO$_3$. *Phys. Rev. B* **96**, 144407 (2017).

34. P. C. Spruijtenburg, "Template controlled octahedral rotations and the metal–insulator transition in SrRuO$_3$," thesis, University of Twente (2011).

35. H. Meley, Karandeep, L. Oberson, J. de Bruijckere, D. T. L. Alexander, J.-M. Triscone, P. Ghosez, S. Gariglio, Structural analysis of LaVO$_3$ thin films under epitaxial strain. *APL Mater.* **6**, 046102 (2018).

36. J. Q. Yan, J. S. Zhou, J. B. Goodenough, Ferromagnetism in LaCoO$_3$. *Phys. Rev. B* **70**, 014402 (2004).

37. M. Raekers, K. Kuepper, S. Bartkowski, M. Prinz, A. V. Postnikov, K. Potzger, S. Zhou, A. Arulraj, N. Stüßer, R. Uecker, W. L. Yang, M. Neumann, Electronic and magnetic structure of RScO$_3$ (R=Sm,Gd,Dy) from x-ray spectroscopies and first-principles calculations. *Phys. Rev. B* **79**, 125114 (2009).

38. D. Fuchs, C. Pinta, T. Schwarz, P. Schweiss, P. Nagel, S. Schuppler, R. Schneider, M. Merz, G. Roth, H. V. Löhneysen, Ferromagnetic order in epitaxially strained LaCoO$_3$ thin films. *Phys. Rev. B* **75**, 144402 (2007).

39. M. R. Fitzsimmons, S. D. Bader, J. A. Borchers, G. P. Felcher, J. K. Furdyna, A. Hoffmann, J. B. Kortright, I. K. Schuller, T. C. Schulthess, S. K. Sinha, M. F. Toney, D. Weller, S. Wolf, Neutron scattering studies of nanomagnetism and artificially structured materials. *J. Magn. Magn. Mater.* **271**, 103–146 (2004).

40. E. J. Guo, J. R. Petrie, M. A. Roldan, Q. Li, R. D. Desautels, T. Charlton, A. Herklotz, J. Nichols, J. van Lierop, J. W. Freeland, S. V. Kalinin, H. N. Lee, M. R. Fitzsimmons, Spatially resolved large magnetization in ultrathin BiFeO$_3$. *Adv. Mater.* **29**, 1700790 (2017).

41. S. G. Jeong, J. Kim, A. Seo, S. Park, H. Y. Jeong, Y.-M. Kim, V. Lauter, T. Egami, J. H. Han, W. S. Choi, Unconventional interlayer exchange coupling via chiral phonons in synthetic magnetic oxide heterostructures. *Sci. Adv.* **8**, eabm4005 (2022).

42. L. G. Parratt, Surface studies of solids by total reflection of X-rays. *Phys. Rev.* **95**, 359–369 (1954).

43. E. J. Guo, R. Desautels, D. Keavney, M. A. Roldan, B. J. Kirby, D. Lee, Z. L. Liao, T. Charlton, A. Herklotz, T. Z. Ward, M. R. Fitzsimmons, H. N. Lee, Nanoscale ferroelastic twins formed in strained LaCoO$_3$ films. *Sci. Adv.* **5**, eaav5050 (2019).

44. N. Lu, P. Zhang, Q. Zhang, R. Qiao, Q. He, H. B. Li, Y. J. Wang, J. W. Guo, D. Zhang, Z. Duan, Z. L. Li, M. Wang, S. Z. Yang, M. Z. Yan, E. Arenholz, S. Y. Zhou, W. L. Yang, L. Gu, C. W. Nan, J. Wu, Y. Tokura, P. Yu, Electric-field control of tri-state phase transformation with a selective dual-ion switch. *Nature* **546**, 124–128 (2017).

45. S. Smadici, P. Abbamonte, A. Bhattacharya, X. F. Zhai, B. Jiang, A. Rusydi, J. N. Eckstein, S. D. Bader, J. M. Zuo, Electronic reconstruction at SrMnO$_3$-LaMnO$_3$ superlattice interfaces. *Phys. Rev. Lett.* **99**, 196404 (2007).

46. J. Nichols, X. Gao, S. Lee, T. L. Meyer, J. W. Freelandet, V. Lauter, D. Yi, J. Liu, D. Haskel, J. R. Petrie, E. J. Guo, A. Herklotz, D. K. Lee, T. Z. Ward, G. Eres, M. R. Fitzsimmons, H. N. Lee, Emerging magnetism and anomalous Hall effect in iridate–manganite heterostructures. *Nat. Commun.* **7**, 12721 (2016).

47. J. E. Hamann-Borrero, S. Macke, W. S. Choi, R. Sutarto, F. He, A. Radi, I. Elfimov, R. J. Green, M. W. Haverkort, V. B. Zabolotnyy, H. N. Lee, G. A. Sawatzky, V. Hinkov, Valence-state reflectometry of complex oxide heterointerfaces. *npj Quantum Mater.* **1**, 16013 (2016).

48. F. M. F. de Groot, M. Grioni, J. C. Fuggle, J. Ghijsen, G. A. Sawatzky, H. Petersen, Oxygen 1s x-ray-absorption edges of transition-metal oxides. *Phys. Rev. B* **40**, 5715–5723 (1989).

49. W. S. Choi, J.-H. Kwon, H. Jeen, J. E. Hamann-Borrero, A. Radi, S. Macke, R. Sutarto, F. He, G. A. Sawatzky, V. Hinkov, M. Kim, H. N. Lee, Strain-induced spin states in atomically ordered cobaltites. *Nano Lett.* **12**, 4966–4970 (2012).

50. E. Benckiser, M. W. Haverkort, S. Bruck, E. Goering, S. Macke, A. Frañó, X. P. Yang, O. K. Andersen, G. Cristiani, H. U. Habermeier, A. V. Boris, I. Zegkinoglou, P. Wochner, H. J. Kim, V. Hinkov, B. Keimer, Orbital reflectometry of oxide heterostructures. *Nat. Mater.* **10**, 189–193 (2011).

51. J. Freeland, J. Liu, M. Kareev, B. Gray, J. W. Kim, P. Ryan, R. Pentcheva, J. Chakhalian, Orbital control in strained ultra-thin LaNiO$_3$/LaAlO$_3$ superlattices. *Europhys. Lett.* **96**, 57004 (2011).

52. Y. Cao, X. Liu, M. Kareev, D. Choudhury, S. Middey, D. Meyers, J.-W. Kim, P. J. Ryan, J. W. Freeland, J. Chakhalian, Engineered Mott ground state in a LaTiO$_{3+\delta}$/LaNiO$_3$ heterostructure. *Nat. Commun.* **7**, 10418 (2016).

53. A. M. Glazer, The classification of tilted octahedra in perovskites. *Acta Crystallogr. B* **28**, 3384–3392 (1972).

54. J. Yamashita, J. Kondo, Superexchange interaction. *Phys. Rev.* **109**, 730–741 (1958).

55. E.-J. Guo, R. Desautels, D. Lee, M. A. Roldan, Z. Liao, T. Charlton, H. Ambaye, J. Molaison, R. Boehler, D. Keavney, A. Herklotz, T. Z. Ward, H. N. Lee, M. R. Fitzsimmons, Exploiting symmetry mismatch to control magnetism in a ferroelastic heterostructure. *Phys. Rev. Lett.* **122**, 187202 (2019).

56. S. Yoon, X. Gao, J. Ok, Z. Liao, M.-G. Han, Y. Zhu, P. Ganesh, M. F. Chisholm, W. S. Choi, H. N. Lee, Strain-induced atomic-scale building blocks for ferromagnetism in epitaxial LaCoO$_3$. *Nano Lett.* **21**, 4006–4012 (2021).

57. Y. Zhang, Y. Si, Y. Jia, P. Yu, R. Yu, J. Zhu, Controlling strain relaxation by interface design in highly lattice-mismatched heterostructure. *Nano Lett.* **21**, 6867–6874 (2021).

58. J. P. Perdew, A. Ruzsinszky, G. I. Csonka, O. A. Vydrov, G. E. Scuseria, L. A. Constantin, X. Zhou, K. Burke, Restoring the density-gradient expansion for exchange in solids and surfaces. *Phys. Rev. Lett.* **100**, 136406 (2008).

59. G. Kresse, J. Furthmüller, Efficient iterative schemes for ab initio total-energy calculations using a plane-wave basis set. *Phys. Rev. B* **54**, 11169–11186 (1996).

60. W. Kohn, L. J. Sham, Self-consistent equations including exchange and correlation effects. *Phys. Rev.* **140**, A1133–A1138 (1965).

61. L. Qiao, J. H. Jang, D. J. Singh, Z. Gai, H. Xiao, A. Mehta, R. K. Vasudevan, A. Tselev, Z. Feng, H. Zhou, S. Li, W. Prellier, X. Zu, Z. Liu, A. Borisevich, A. P. Baddorf, M. D. Biegalski, Dimensionality controlled octahedral symmetry-mismatch and functionalities in epitaxial LaCoO$_3$/SrTiO$_3$ heterostructures. *Nano Lett.* **15**, 4677–4684 (2015).

62. B. J. Campbell, H. T. Stokes, D. E. Tanner, D. M. Hatch, ISODISPLACE: A web-based tool for exploring structural distortions. *J. Appl. Cryst.* **39**, 607–614 (2006).

63. H. T. Stokes, S. van Orden, B. J. Campbell, ISOSUBGROUP: An internet tool for generating isotropy subgroups of crystallographic space groups. *J. Appl. Cryst.* **49**, 1849–1853 (2016).

64. H. N. Lee, H. M. Christen, M. F. Chisholm, C. M. Rouleau, D. H. Lowndes, Strong polarization enhancement in asymmetric three-component ferroelectric superlattices. *Nature* **433**, 395–399 (2005).

Atomically engineered cobaltite layers for robust ferromagnetism

Shengru ChenQinghua ZhangXujing LiJiali ZhaoShan LinQiao JinHaitao HongAmanda HuonTimothy CharltonQian LiWensheng YanJiaou WangChen GeCan WangBaotian WangMichael R. FitzsimmonsHaizhong GuoLin GuWen YinKui-juan JinEr Jia Guo

View the article online
https://www.science.org/doi/10.1126/sciadv.abq3981
Permissions
https://www.science.org/help/reprints-and-permissions

Use of this article is subject to the Terms of service